Nuclear Science and Techniques (2025) 36:79
https://doi.org/10.1007/s41365-025-01658-8

Integrated multi-scale synchrotron radiation-technology studies on $AlPO_4$-coating modification mechanism in lithium-rich manganese-based cathode

Zhong-Qin Dai[1,2] · **Huan Chen**[2,3] · **Zhao-Yin Wen**[1,2,3]

Received: 23 August 2024 / Revised: 16 October 2024 / Accepted: 21 October 2024 / Published online: 20 March 2025

Abstract

Lithium- and manganese-rich (LMR) oxide cathode materials are among the most attractive candidates for next-generation energy-storage materials owing to their anomalous capacity. However, severe Mn dissolution that occurs during long-term cycling, which leads to capacity loss, hinders their application prospects. In this study, nanoscale $AlPO_4$-coated $Li_{1.2}Ni_{0.13}Co_{0.13}Mn_{0.54}O_2$ (LMR@APO) with significantly enhanced electrochemical performance is successfully synthesized using a simple and effective sol–gel method to mitigate Mn dissolution and suppress local structural distortion at high voltages. Because of the complex evolution of the structure and oxidation state of LMR materials during electrochemical cycling, observing and analyzing them using traditional single characterization methods may be difficult. Therefore, we combine various synchrotron-based characterization techniques to conduct a detailed analysis of the electronic and coordination structures of the cathode material from the surface to the bulk. Synchrotron-based hard and soft X-ray spectroscopies are integrated to investigate the differences in O and Mn evolution between the surfaces and bulk of the cathode. Advanced synchrotron-based transmission X-ray microscopy combined with X-ray near-edge absorption-structure technology is utilized to visualize the two-dimensional nanometer-scale reactivity of the LMR cathode. The $AlPO_4$-coating layer can stabilize the surface structure of the LMR material, effectively alleviating irreversible oxygen release on the surface and preventing the dissolution of Mn^{2+} at the interface caused by side reactions after a long cycle. Therefore, the spatial reaction uniformity of Mn is enhanced by the $AlPO_4$-coating layer, and rapid capacity decay caused by Mn deactivation is prevented. The $AlPO_4$-coating method is a facile modification strategy for high-performance LMR materials.

Keywords Synchrotron radiation · X-ray absorption fine structure · X-ray imaging · Amorphous coating layer · Lithium- and manganese-rich (LMR) cathode

1 Introduction

The increasing demand for electric vehicles and consumer electronics has increased the required energy density of lithium-ion batteries (LIBs). The key to breakthroughs in LIB materials lies in improving the performance of cathode materials [1, 2]. Lithium- and manganese-rich (LMR) oxide cathode materials, especially those with an elemental composition of $Li_{1.2}Ni_{0.13}Co_{0.13}Mn_{0.54}O_2$, are promising candidates owing to their substantially higher energy densities and high operating voltages and have been investigated extensively in the past two decades. LMR materials are layered materials comprising $LiMO_2$ (M=Ni, Co, Mn) and Li_2MnO_3 phases [3]. The anomalous specific capacity of Li-rich Mn-based cathode materials originates from the

This work was supported by the National Key R&D Program of China (No. 2022YFB3807700), National Natural Science Foundation of China (Nos. U20A20248 and 52372247), Shanghai Pujiang Programme (23PJD110), and Science and Technology Commission of Shanghai Municipality (No. 18DZ2280800).

✉ Zhao-Yin Wen
zywen@mail.sic.ac.cn

[1] School of Physical Science and Technology, ShanghaiTech University, Shanghai 201210, China

[2] The State Key Lab High-Performance Ceram & Superfine, Shanghai Institute of Ceramics, Chinese Academy of Sciences, Shanghai 200050, China

[3] University of Chinese Academy of Science, Beijing 100049, China

activation of anionic redox reactions at high operating potentials, which far exceeds that of the cationic redox reactions in conventional layered oxide electrodes [4]. However, several unfavorable properties, such as voltage hysteresis and degradation in voltage and capacity, hamper their practical application [5]. The inevitable dissolution of Mn from cathode materials is an important factor during electrochemical cycling [6]. Mn dissolution in the cathode side can lead to severe structural rearrangement and rapid capacity decay [7]. Moreover, the product of Mn dissolution can attack PF^{6-} in the electrolyte and affect the stability of the formed solid electrolyte interphase driven by the electric field [8]. The critical impact of Mn dissolution on the cycling performance of LMR materials has motivated researchers to explore its mechanisms and modification strategies to mitigate dissolution [6].

During the electrochemical cycling process, the surface Mn is reduced from a higher oxidation state to Mn^{3+} because of the activation of the $Mn^{3+/4+}$ couple triggered by irreversible oxygen loss upon the first charge [5, 9]. Moreover, Mn^{3+} undergoes disproportionation to generate Mn^{2+} because of the Jahn–Teller effect, which ultimately leads to the dissolution of Mn on the material surface in the form of Mn^{2+} in the electrolyte [10]. Various strategies have been developed to address this challenge based on research on the Mn dissolution mechanism. Surface-coating layers with metal oxides, fluorides, and fast lithium-ion conductors using chemical methods have been developed to contribute to the stability of the Mn valence and mitigation of Mn^{2+} dissolution [11, 12].

Despite improvements achieved by these surface modification strategies, a detailed understanding of the underlying mechanisms is still lacking. This is because the regulation of electrochemical performance in LMR materials typically involves complex, simultaneous changes in the electronic and short-range ordered structures of the material with spatial heterogeneity, making observations with single traditional characterization methods difficult. Furthermore, traditional characterization methods are limited by resolution and penetrability and cannot accurately obtain key structural information of the multiscale changes in cathode materials [7, 13]. Advanced synchrotron-based techniques allow for the simultaneous acquisition of coupled electronic and structural information through the interaction of precisely tuned X-rays with materials, thereby elucidating complex changes within LMR materials [14]. Moreover, different synchrotron radiation technologies can complement and corroborate each other, such as obtaining detailed information about the material surface through soft X-ray absorption spectroscopy (sXAS), obtaining detailed information about the material bulk through hard X-ray absorption spectroscopy (hXAS), and using synchrotron radiation X-ray imaging technology to obtain spatial structural information of the material [15–18]. Therefore, the combination of multiple synchrotron radiation technologies can fully reveal the specific mechanisms of LMR materials [19].

Herein, we demonstrate a simple and efficient sol–gel method for forming an amorphous $AlPO_4$ coating on $Li_{1.2}Ni_{0.13}Co_{0.13}Mn_{0.54}O_2$ (LMR) oxide cathode materials. Characterizations combining various synchrotron radiation techniques were conducted at the Shanghai Synchrotron Radiation Facility (SSRF) [20, 21] to elucidate the specific mechanism of this modification method in detail. sXAS is used for studying surface structures, hXAS for examining bulk phases, and transmission X-ray microscopy combined with X-ray near-edge absorption-structure (TXM-XANES) technology for visualizing the two-dimensional (2D) valence-state distribution of Mn. The formation and dissolution processes of Mn^{2+} on the material surface are characterized in detail. The correlation between the anionic oxidation reactions on the surface and in the bulk phase with Mn dissolution is studied simultaneously using the combined total electron yield (TEY) and total fluorescence yield (TFY) modes of sXAS. A comprehensive analysis of the Mn dissolution process elucidates the mechanism by which the $AlPO_4$ coating inhibits Mn disproportionation and mitigates structural degradation and Mn dissolution during cycling.

2 Experimental section

2.1 Material preparation

Pristine $Li_{1.2}Ni_{0.13}Co_{0.13}Mn_{0.54}O_2$ material was purchased from Fuli. The $AlPO_4$-coated $Li_{1.2}Ni_{0.13}Co_{0.13}Mn_{0.54}O_2$ material was synthesized using a facile sol–gel method. Different concentrations of phosphorus pentoxide (P_2O_5, 99.99%, Aladdin) and aluminum nitrate hydrate ($Al(NO_3)_3 \cdot 9H_2O$, analytical reagent, Sinopharm) were dissolved in ethanol. Ammonium bicarbonate (NH_4HCO_3, reagent grade, Aladdin) was used to adjust the pH to 7, and the solution was stirred at 60 °C for 3 h. Salting-out was carried out at −10 °C using liquid nitrogen, and the mother liquor was collected after filtration. Pristine $Li_{1.2}Ni_{0.13}Co_{0.13}Mn_{0.54}O_2$ material was added and stirred at 80 °C for 3 h to obtain the LMR@APO precursor. This precursor was sintered in a muffle furnace at 400 °C for 4 h to obtain the $Li_{1.2}Ni_{0.13}Co_{0.13}Mn_{0.54}O_2$ material coated with $AlPO_4$. Only the amounts of $Al(NO_3)_3 \cdot 9H_2O$ and P_2O_5 need to be changed to obtain $Li_{1.2}Ni_{0.13}Co_{0.13}Mn_{0.54}O_2$ materials with different $AlPO_4$ coating contents.

2.2 Material characterizations

Scanning electron microscopy (SEM; S-4800N, Hitachi, Japan) and energy-dispersive X-ray spectroscopy (EDS) mapping was performed to observe the morphology of the samples. High-resolution transmission electron microscopy (HRTEM) was conducted using a transmission electron microscope (G2 F20 S-TWIN, Tecnai FEI, USA). X-ray diffraction (XRD) measurements were taken for phase analysis (D8 Advance X, Bruker, USA; Cu-Kα radiation, λ=1.542 Å) in the 2θ range of 10–80° at room temperature. X-ray photoelectron spectroscopy (XPS; ESCALAB250 Thermo Fisher, USA) was performed to determine the elemental composition of the samples. The ex-situ hXAS test for the Mn K-edge of the LMR sample was performed at the Shanghai Synchrotron Radiation Facility (SSRF) BL16U1 beamline, with a photon flux of 3.7×10^{12} photons s^{-1} at the sample position, using the transmission mode [20]. The hXAS test for the Mn K-edge of the long cycling LMR samples was performed at the SSRF BL14W beamline with a photon flux of 2.6×10^{12} photons s^{-1} at the sample position using the transmission mode [23]. The ex-situ hXAS tests for the Ni K-edge and Co K-edge of the LMR sample were performed at the SSRF BL20U1 beamline with a photon flux of 10^{12} photons s^{-1} at the sample position using the fluorescence mode [24]. All the hXAS tests were calibrated using the K-edge data of the transition-metal foils corresponding to the tested elements. The Mn L-edge sXAS of the LMR sample was obtained at the SSRF BL08U1A beamline using the TEY mode with photon fluxes of 1.5×10^8 photons s^{-1} and an approximate pressure of 10^{-6} Torr [25, 26]. Calibration was performed using Mn L-edge data of the standard MnO_2 sample. The O K-edge sXAS was performed at the SSRF BL02B02 beamline using a combination of the TEY and TFY modes with a photon flux at the sample position of 3×10^{10} photons s^{-1} and an approximate pressure of 5×10^{-9} Torr [27]. Calibration was performed using the O K-edge data of the standard $SrTiO_3$ sample. The XAS data were processed using Athena software from the IFEFFIT software package for energy calibration, noise removal, background subtraction, and normalization [28]. Wavelet transform analysis was performed using wtEXAFS software. The Mn K-edge TXM-XANES test of the LMR samples was carried out at the SSRF BL18B beamline, with a photon flux of 1.3×10^{10} photons s^{-1} at the sample position, field of view of approximately 20 µm × 20 µm, and spatial resolution of 60 nm [29]. The active material from the electrode sheet was obtained from batteries disassembled in an argon-filled glove box. The material was scraped off with a scalpel and then placed in a blue-capped vial, and dimethyl carbonate (DMC) solvent was added. After sealing, the blue-capped vial was removed from the glove box for ultrasonication. Finally, before testing, the sample was delivered to the microtip of the glass tube using an industrial dispenser.

2.3 Electrode preparation and cell assembly

Electrochemical performance tests were conducted using coin-type 2025 cells. Both cathode materials were composed of a mixture containing 80 wt% active material and 10 wt% poly (vinylidene difluoride) binder in a precise amount of N-methyl-2-pyrrolidone (NMP), 5 wt% Super P, and 5 wt% vapor-grown carbon fiber. The resulting slurry was uniformly cast onto aluminum foil and dried overnight at 70 °C under vacuum conditions to remove the NMP. Then, disk electrodes with a diameter of 12 mm were punched from the coated foil, achieving an average active material mass loading of 2.5–3.5 mg cm^{-2}. Half-cell assembly was performed in an argon-enriched glovebox to ensure a contamination-free environment, utilizing pure lithium as the counter electrode. A polypropylene membrane (Celgard-2400) was used as the separator. The electrolyte solution consisted of 1 M LiPF6 dissolved in a mixture of ethylene carbonate, DMC, and diethyl carbonate in a volumetric ratio of 1:1:1. Precisely 100 μL of this type of electrolyte was added to each coin cell to maintain a uniform electrochemical behavior.

2.4 Electrochemical measurements

All measurements for the electrochemical testing of the coin-type cells were performed at ambient room temperature. Galvanostatic cycling tests were performed at a constant current density of 1 C (1 C = 250 mA h g^{-1}) over 2.0–4.6 V using a NEWARE battery-testing system.

3 Results and discussion

The initial charge–discharge curves of the pristine $Li_{1.2}Ni_{0.13}Co_{0.13}Mn_{0.54}O_2$, as well as those encapsulated with different amounts of $AlPO_4$ coating at a 0.1 C rate, are shown in Figure S1 (Supporting Information). All the samples exhibit similar charge–discharge profiles. Comparing the discharge capacity of the first cycle, the $Li_{1.2}Ni_{0.13}Co_{0.13}Mn_{0.54}O_2$ sample coated with 0.5 wt% $AlPO_4$ achieves a value of 305.77 mA h g^{-1}, whereas the other samples demonstrate significantly lower discharge capacities. Figure S2 illustrates the cycling performance of all samples at an electric current of 1 C. Clearly, the sample coated with 0.5 wt% $AlPO_4$ exhibits superior cycling stability and capacity retention after 200 cycles compared to the uncoated material, the mixture of LMR and $AlPO_4$, and those coated with 1.0 wt% and 2.0 wt% $AlPO_4$.

Based on these observations, the 0.5 wt% $AlPO_4$-coated material demonstrates the best electrochemical performance. Consequently, we only examine the pristine and 0.5 wt% $AlPO_4$-coated LMR samples (designated as LMR@0.5% APO) in the following analysis.

3.1 Structure and morphology of $AlPO_4$-coated LMR material

The XRD patterns of pristine, 0.5 wt% $AlPO_4$-, 1 wt% $AlPO_4$-, and 2 wt% $AlPO_4$-coated LMR samples are shown in Figs. 1a and S3. The patterns can be indexed with the O3-type layered structure of the hexagonal α-$NaFeO_2$, featuring an $R\bar{3}m$ space group. The additional reflections between 20° and 25°, corresponding to a weak superlattice, are attributed to the (020) and (110) lattice planes of the Li_2MnO_3-like component with a $C2/m$ space group. This implies the existence of a honeycomb-like short-range ordered structure of $LiMn_6$ in the transition-metal (TM) layers. The observed separation of the (006)/(012) and (018)/(110) peaks indicates a well-crystallized layered structure in the lattice [22]. Compared to the original sample, coated samples exhibit similar diffraction peaks, indicating no significant change in the bulk structure. The fine-scanned XRD patterns of samples with different coating amounts at positions corresponding to the $AlPO_4$ reflection peaks are displayed in Fig. S4. No obvious reflections are observed owing to the amorphous state and low coating amount of the $AlPO_4$ coating layer. This means that the sample coated with $AlPO_4$ maintains the intact hexagonal α-$NaFeO_2$ structure with good arrangement after surface modification. Additionally, XPS measurements are conducted to provide more evidence of the successful modification of $AlPO_4$. The photoemission peaks of Al 2P and P 2p detected on the LMR@0.5% APO sample are illustrated in Fig. 1b, c. The Al 2p binding energy, measured at 73.4 eV, is between the reported values for the $AlPO_4$ material at 74.5 eV and the range observed for materials such as $LiAl_xM_{1-x}O_2$ (M = Co, Ni) [30]. This may be attributed to the diffusion of Al after the calcination process, resulting in the formation of a solid solution at the interface of the coating layer and underlying bulk material [31]. The P 2p photoemission peak is divided into two components at 134.5 eV and 133.2 eV, which are consistent with the reports of $AlPO_4$ and Li_3PO_4, confirming the presence of the $AlPO_4$ phase and accompanying Li_3PO_4 phase on the sample surface [31]. SEM images displayed in Fig. 1d, e reveal that both pristine and 0.5 wt% $AlPO_4$-coated LMR materials exhibit comparable morphology, suggesting that the coating process does not alter the morphology of the particles. The spherical particles, approximately 10 micrometers in diameter, consist of uniform primary nanoparticles. Figure 1f and S5 demonstrate the even distribution of Al, P, and O in the EDS elemental-mapping images, demonstrating the successful encapsulation of $AlPO_4$.

TEM was also employed to further observe the $AlPO_4$ coating layer. In Fig. 1g, h, TEM images of both the pristine and 0.5 wt% $AlPO_4$-coated LMR samples show well-defined equidistant fringes. This corresponds to a d-spacing of 0.47 nm on the (003) plane, indicating good crystallinity in bulk crystal [32]. The TEM image of the 0.5 wt% $AlPO_4$-coated LMR sample shows an approximately 8-nm-thick coating layer within an amorphous phase. Additionally, this coating layer is uniformly distributed across the surface of the bulk material.

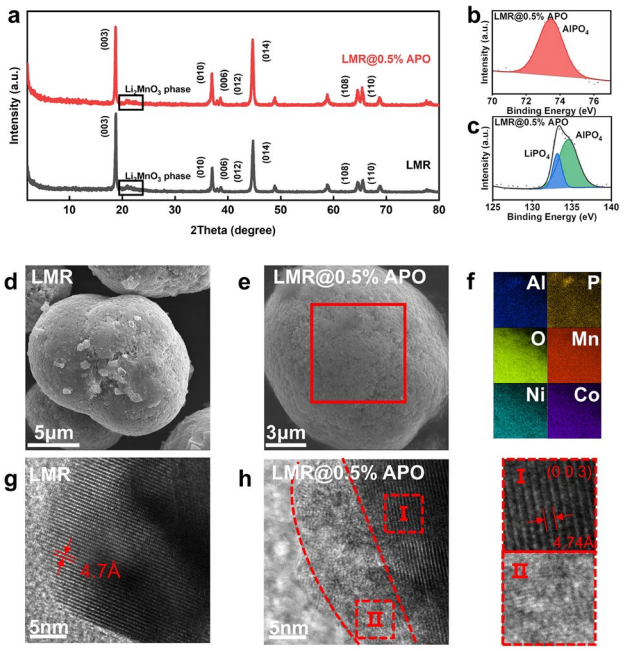

Fig. 1 (Color online) **a** XRD patterns of pristine LMR and LMR@0.5% APO samples. **b** P 2p and **c** Al 2p XPS spectra of LMR@0.5% APO sample. SEM images of **d** pristine and **e** LMR@0.5% APO samples. **f** EDS element mapping of the LMR@0.5% APO sample. HRTEM images of **g** pristine LMR and **h** LMR@0.5% APO samples

3.2 Electrochemical performance measurements

The electrochemical performances of both the pristine and 0.5 wt% $AlPO_4$-coated LMR samples are shown in Fig. 2. Figure 2a compares the cycling performances of pristine and LMR@0.5% APO samples with different coating amounts at a 1 C rate. To fully activate the lithium-rich manganese material, a low rate of 0.1 C was employed for the first two cycles, with a working-voltage range set between 2.0 and 4.7 V. For subsequent cycles, a 1 C rate was employed with a working-voltage range set between 2.0 and 4.6 V. The pristine LMR sample has an initial discharge specific capacity of 293.43 mA h g^{-1}; however, it begins to decay sharply after approximately 100 cycles,

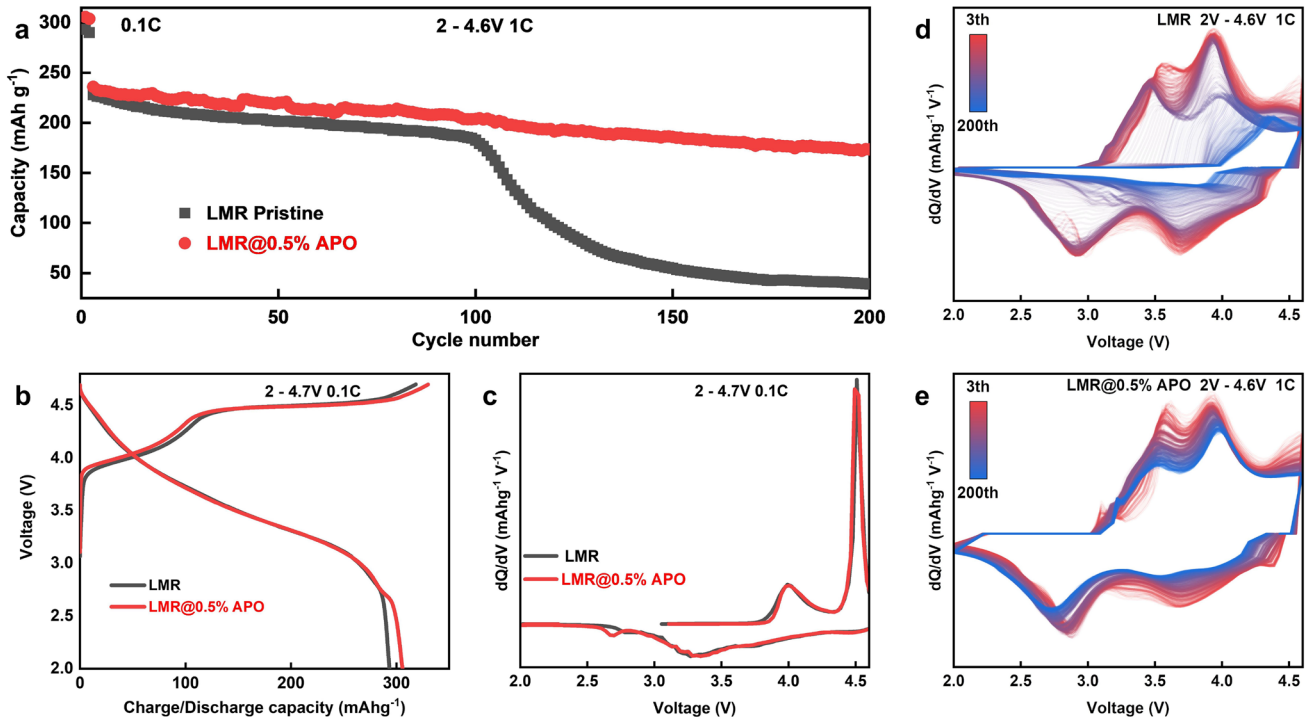

Fig. 2 (Color online) **a** Cycle performance of pristine LMR and LMR@0.5% APO samples at 1 C. **b** Initial charge and discharge curves (at 0.1 C). **c** dQ/dV profiles (at 0.1 C). dQ/dV profiles from the 3rd to 200th cycle at 1 C of **d** pristine LMR and **e** LMR@0.5% APO samples

and the capacity is only 39.12 mA h g^{-1} after 200 cycles. The LMR@0.5% APO sample exhibits enhanced cycling stability and specific capacity during cycling, with an initial discharge specific capacity of 305.77 mA h g^{-1}. After 200 cycles at 1 C, the capacity remains at 173.36 mA h g^{-1}, with a capacity retention rate of 73.9% relative to the third cycle at the beginning of the 1 C cycling. This is because the side reactions caused by the complete exposure of the pristine LMR material surface to the electrolyte, the irreversible structural phase changes on the surface of the LMR material, and local structural distortion at high voltages during the cycling process are suppressed by the $AlPO_4$ coating layer. Figure 2b presents the initial charge–discharge curve of the pristine and 0.5 wt% $AlPO_4$ -coated LMR samples at 0.1 C (1 C = 250 mA h g^{-1}) within the voltage range of 2.0−4.7 V. The initial charge curve is characterized by a sloping section below 4.4 V and plateau above 4.5 V. This lower sloping section is associated with the oxidation of Co^{3+} and Ni^{2+} ions. The plateau above 4.5 V corresponds to the phase transition involving the anionic redox reaction, which is typically accompanied by the liberation of oxygen [33, 34]. The pristine LMR sample exhibits an initial charging capacity of 318.45 mA h g^{-1} at 0.1 C; however, it incurs a substantial irreversible capacity of 25.22 mA h g^{-1}. The specific initial discharge capacity is 293.43 mA h g^{-1}, with a Coulombic efficiency of 92.1% for the initial cycle. Conversely, the 0.5 wt% $AlPO_4$-coated LMR sample presents an initial discharge capacity of 305.77 mA h g^{-1}, along with an improved Coulombic efficiency of 92.6%. This enhancement suggests that the $AlPO_4$ coating effectively stabilizes the surface of the sample. It also mitigates the irreversible loss of lattice oxygen and curtails side reactions at the electrode–electrolyte interface, which contribute to capacity decline [35], thereby improving the initial discharge capacity and overall Coulombic efficiency. To further investigate the electrochemical reactions throughout the charge and discharge cycles, the corresponding differential capacity versus voltage (dQ/dV) curves and charge–discharge curves of both samples at different numbers of cycles are shown in Fig. 2c and S6. The LMR samples do not exhibit significant differences in the overall distribution of the peak profiles after the coating modification before approximately 100 cycles. The first peak at 4.05 V is attributed to the oxidation of Ni^{2+}/Ni^{4+} and Co^{3+}/Co^{4+}, and the second peak at 4.5 V is attributed to the anionic oxidation in the initial charge process. Owing to the inversion of cationic and anionic redox reactions, the first peak at 4.3 V is attributed to the reduction of the transition metal, whereas the second peak at approximately 3.3 V is attributed to the reduction of anionic ligands and the reduction of Mn^{4+} to Mn^{3+} owing to the loss of O_2 [9] during the discharge process. The additional reduction peak at 2.75 V is due to lithium-ion

intercalation of the spinel phase. This indicates the formation of a spinel phase on the surface during the coating process [36], which can be substantiated by subsequent sXAS analysis. The dQ/dV plots of the subsequent cycles indicate that after 100 cycles, the oxidation peak of the pristine LMR sample significantly shifts to the right and the reduction peak significantly shifts to the left, suggesting that substantial polarization affects the progression of redox reactions and leads to rapid capacity decrease. In contrast, the 0.5 wt% $AlPO_4$-coated LMR sample maintains good electrochemical activity with no significant shifts in the positions of the oxidation and reduction peaks, demonstrating the well-maintained structure because of the $AlPO_4$ coating.

3.3 Electronic structure characterized by combined synchrotron-based X-ray absorption spectroscopy

To further explore the modification mechanism of $AlPO_4$ coatings on LMR materials, ex-situ synchrotron-based sXAS and hard-XANES technology is employed to investigate the evolution of surface and bulk Mn in the LMR materials during the electrochemical cycling process. The hard-XANES test was performed at beamline BL20U of the SSRF using the transmission mode [24]. The transmission mode involves the ratio of the ionization-chamber currents before and after the sample, reflecting the interaction between the X-rays and material. Through hard-XANES testing, we can obtain information about the lowest unoccupied states of the 3d transition-metal elements in the bulk of the material and determine their average oxidation states [37–39]. The sXAS test was performed at beamline BL08U1A of the SSRF using the TEY mode. In the TEY mode, we can measure the photogenerated current on the material surface using a picoammeter and determine the transition of 3d transition-metal elements from the 2p states to 3d states. Because information on the unoccupied 3d orbital states is directly related to the electrochemical performance of cathode materials, sXAS can provide strong support for the study of cathode materials [40, 41]. As shown in Fig. 3b, during the charging process, the white-line peak of the Mn K-edge shifts marginally to the right-hand side, whereas the half-height energy moves to the left-hand side. Because of the complexity of the Mn K-edge spectrum, the oxidation state of Mn cannot be determined accurately. The position of the K absorption edge corresponds to the transition from the Mn 1 s orbital to the first dipole-allowed transition orbital; therefore, a significant enhancement in the absorption intensity occurs at the edge position. Therefore, the absorption edge can be accurately determined by identifying the position of the strongest peak in the first derivative, thereby determining the oxidation state. During the charging process, the maximum value of the first derivative, which is the position of the absorption edge, undergoes a slight shift to the right-hand side of less than 2 eV, which may be owing to the oxidation

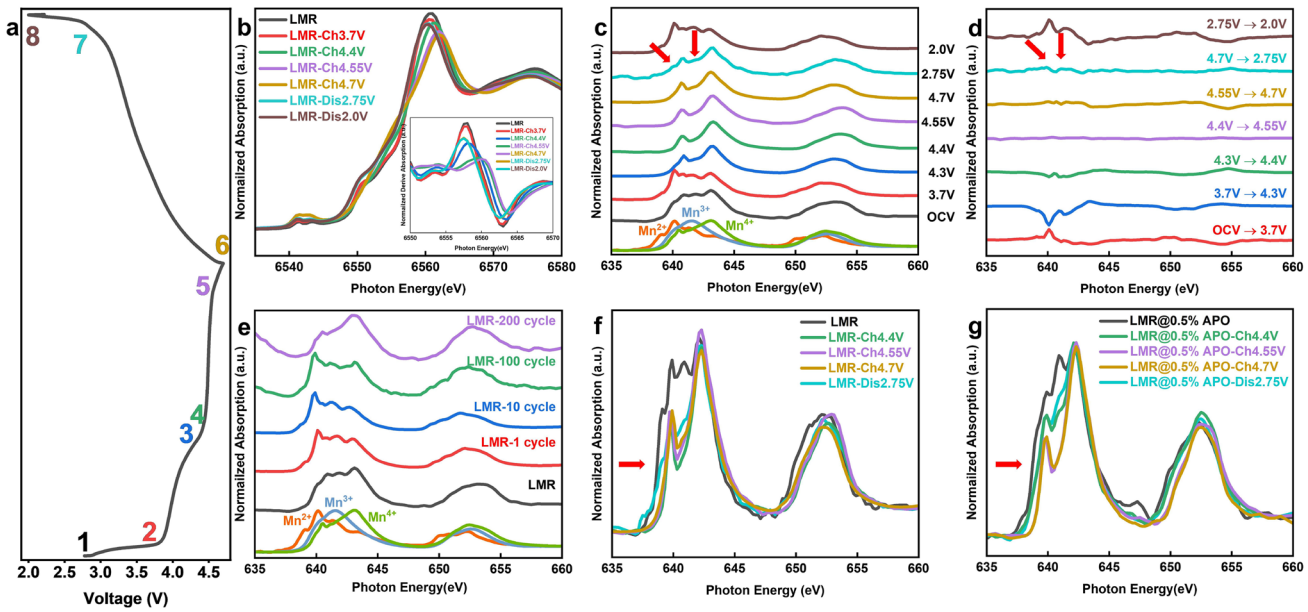

Fig. 3 (Color online) (a) Electrochemical curve of LMR material under ex-situ X-ray absorption spectrum. (b) Ex-situ XANES spectra at Mn K-edge for pristine LMR sample during the first cycle. (c) Ex-situ XANES spectra at Mn L-edge for pristine LMR sample during the first cycle. (d) Differential spectrum of ex-situ XANES spectra at the Mn L-edge for pristine LMR sample during the first cycle. (e) XANES spectra at Mn L-edge for pristine LMR sample after 200 cycles. Ex-situ XANES spectra of the evolution of Mn for (f) pristine LMR and (g) LMR@0.5% APO samples

of low-valence Mn produced by element segregation during the sample-synthesis process. When discharged to 2.75 V, the Mn K-edge XANES spectrum shifts significantly back toward the pristine position, corresponding to the reduction of Mn on the surface during discharge. Notably, in the parts of the charge–discharge curves where the capacity is not provided, specifically during charging from OCV to 3.7 V and discharging from 2.75 to 2 V, no significant shift in the Mn K-edge XANES is observed, indicating that the average valence state does not significantly change during these processes. The ex-situ sXAS spectrum in Fig. 3c shows that when charging from OCV to 3.7 V, a marked decrease occurs in the valence state of surface Mn from approximately Mn^{4+} to Mn^{2+}. This valence state remains at approximately +4 during the charging plateau above 4.4 V. Upon discharging to 2.75 V, features of Mn^{2+} and Mn^{3+} reemerge, which corresponds to the reduction of Mn^{4+} observed in the dQ/dV plots. Further discharge to 2.0 V results in a rapid reduction of the surface valence state to Mn^{2+}. This evolutionary trend is clearly demonstrated in the differential spectrum shown in Fig. 3d. Integrating the analysis of differences in Mn signals between the bulk and surface indicates that the surface Mn^{2+} is primarily generated in the low-voltage sloped sections of the electrochemical curves, where no capacity is provided, as the average valence state of Mn in the bulk remains unchanged. This suggests that the significant surface enrichment of Mn^{2+} results from intrinsically chemical reactions, rather than electrochemical reactions. Furthermore, this observation aligns with findings in the literature that a weakly acidic $LiPF_6$ electrolyte promotes the disproportionation of Mn^{3+} to form Mn^{4+} and the more soluble Mn^{2+}, which is more likely to be desorbed and adsorbed on the surface [21]. This further supports the hypothesis of chemically driven changes in Mn valence at the surface during electrochemical cycling. Subsequently, we tracked the evolution of surface Mn during extended cycling. As shown in Fig. 3e, the surface Mn oxidation state was consistently at +2 before the rapid capacity decline (within 100 cycles), and it then increased to +4 after 200 cycles. This is attributed to ongoing disproportionation reactions at the surface during electrochemical cycling, where Mn^{4+} ions are retained on the surface and Mn^{2+} ions are solubilized. This disrupts the electrolyte and leads to interference between the anode and cathode. This disproportionation reaction leads to increased polarization and renders the material electrochemically inactive, triggering a rapid capacity decrease. After 200 cycles, the surface Mn^{2+} is completely solubilized in the electrolyte, and the surface signal of the sample is dominated by Mn^{4+} [7]. The improvement mechanism of the $AlPO_4$-coating layer is then investigated. By utilizing ex-situ Mn L-edge XANES, the evolution of Mn on the surfaces of pristine LMR and LMR@0.5% APO samples is compared in Fig. 3f and g, which show distinct differences. Firstly, the feature peak corresponding to Mn^{3+} in the coated sample before cycling is significantly stronger than that in the pristine sample, indicating the formation of a spinel-like phase on the surface owing to the coating process. During the charging process, the coated sample exhibits a slower rate of Mn oxidation. This suggests that the $AlPO_4$-coating layer can modulate the reaction degree, thereby suppressing the overcharge and surface structural changes related to high-voltage oxygen release. Furthermore, when charged to 4.7 V, a small Mn^{3+} signal appears on the surface of the pristine LMR sample, corresponding to the so-called reductive elimination mechanism, where surface transition metals are reduced owing to oxygen release at high charging states. The oxygen-deficient surface structure results from the irreversible release of oxygen, which causes a more severe reduction of Mn at low voltages. In contrast, the LMR@0.5% APO sample maintains Mn^{4+} on its surface when charged to 4.7 V, indicating that the $AlPO_4$-coating layer effectively stabilizes the surface structure, suppresses surface oxygen evolution, and enhances the initial Coulombic efficiency [42]. Finally, when discharged to 2.75 V, no Mn^{2+} signal is detected, even though the coated sample surface similarly presents the Mn^{3+} signal resulting from the reduction of Mn^{4+}. Moreover, an Mn^{2+} signal can be clearly observed in the Mn L-edge sXAS of the cycled LMR@0.5% APO sample (Fig. S7), which is different from that of the cycled LMR sample. This implies that the $AlPO_4$-coating layer effectively obstructs the direct interaction between the electrode and electrolyte [10, 43]. This inhibits side-reaction-induced Mn disproportionation and significantly mitigates the capacity decay caused by Mn^{2+} dissolution, which enhances the cycle stability.

Extended X-ray absorption fine structure (EXAFS) spectroscopy was used to investigate changes in the bulk average oxidation states and local coordination environments of pristine LMR and LMR@0.5% APO during long-term cycling. The EXAFS and XANES testing methods are similar, but the EXAFS test requires scanning over a wider energy range. Through EXAFS testing, we can simultaneously obtain information on the nearest-neighbor coordination and oxidation state of 3d transition-metal elements. This is important for cathode materials that undergo severe local structural distortion and changes in oxidation states during the long cycling process [44–46]. As shown in Fig. 4a, b, the Mn K-edge white-line peak of the pristine LMR sample shifts to the right-hand side, whereas that of the LMR@0.5% APO sample shifts to the left-hand side, indicating that the coating modification alters the evolution trend of the bulk oxidation state and local structure of the material during long cycling processes. The first derivative plot of XANES is also presented to obtain oxidation-state information more precisely through the position of the absorption edge. The Mn K-edge of the pristine LMR sample clearly shifts to the

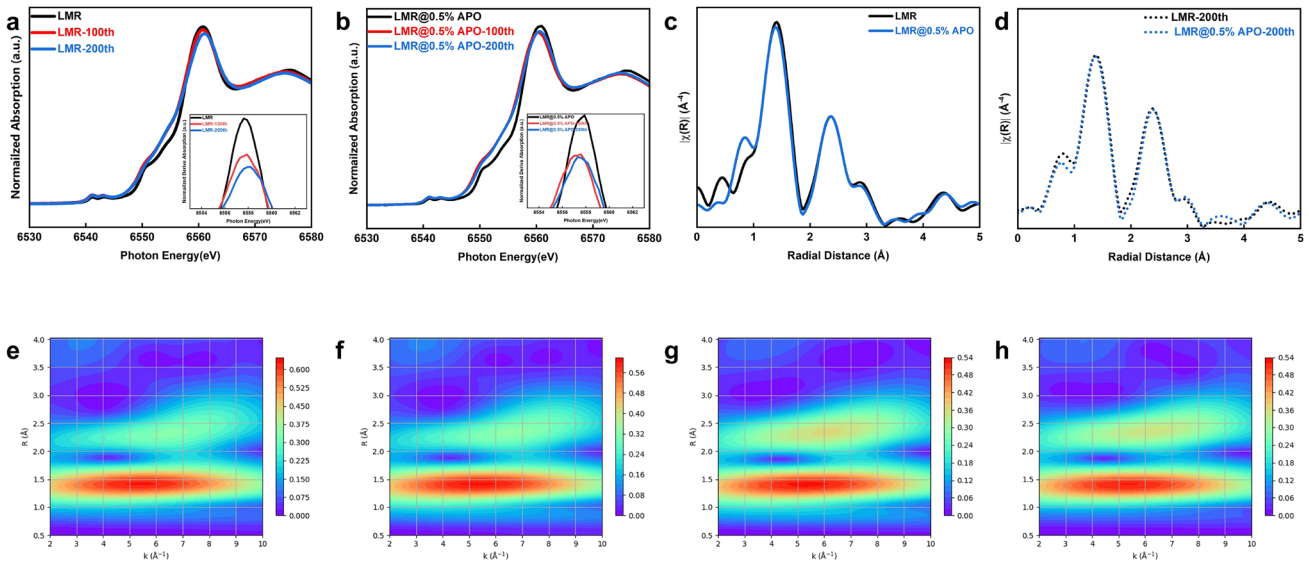

Fig. 4 (Color online) XANES spectra at Mn K-edge of pristine and cycled **a** LMR and **b** LMR@0.5% APO samples. FT-EXAFS of pristine and cycled **c** LMR and **d** LMR@0.5% APO samples. Wavelet transform of **e** pristine LMR and **f** LMR after 200 cycles; wavelet transform of **g** pristine LMR@0.5% APO and **h** LMR@0.5% APO after 200 cycles

right-hand side, indicating an increase in the overall oxidation state of the sample during the long cycling process. However, the Mn K-edge of the LMR@0.5% APO sample exhibits a slight shift to the left-hand side, suggesting that its structure is well maintained during the long cycling process, with only minor electrochemical degradation occurring. However, compared with the obvious changes in the oxidation state of Mn on the surface, the change in the Mn K-edge in the bulk is less than 1 eV. Therefore, the Fourier transform (FT) EXAFS (Fig. 4c, d) and wavelet transform analysis (Fig. 4e, f, g, h) of the pristine and LMR@0.5% APO samples are employed. The results show that the Mn-coordination structures in the bulk phase of both the coated and pristine samples demonstrate no significant differences in the bond lengths and coordination numbers corresponding to the Mn-O and Mn-TM shells after long-term cycling. This difference in the evolution of Mn in the bulk oxidation state and local structure indicates that the spatial uniformity of the Mn reaction during the extended cycling process is a key factor affecting cycling performance.

3.4 Revealing the reaction homogeneity through synchrotron-based transmission X-ray microscopy technique combined with XANES spectroscopy

By employing synchrotron-based TXM-XANES testing at beamline BL18B of the SSRF, the spatial distribution of the Mn-related oxidation state was visualized at the nanoscale, allowing for direct observation of the evolution uniformity of the Mn-related oxidation state. This can be used to study the degradation mechanisms of LMR materials during the long cycling process as well as the modifying effects of the $AlPO_4$-coating layer on these materials. TXM-XANES is a synchrotron-based imaging method that integrates TXM with XANES. The spatial distribution of the oxidation states of micrometer-scale cathode materials can be characterized using X-rays with continuously varying energy for the transmission imaging of materials. This approach overcomes the limitations of traditional approaches, which may neglect detailed characterization by examining only specific areas or averaging values across the entire sample, potentially missing localized changes [29, 47]. The 2D TXM-XANES mapping offers a detailed aging-state analysis for each element by tracking the shifts in their respective XANES spectra [48]. Figure 5a, d shows that the pristine LMR and LMR@0.5% APO samples exhibit a relatively uniform distribution of Mn oxidation states before cycling, with no local enrichment of Mn elements in a particular oxidation state. As shown in Fig. 5b, e, the oxidation-state distributions of the pristine LMR and LMR@0.5% APO samples evolved based on different trends after long-time cycling. Moreover, Fig. S8 illustrates that the average XANES curves extracted from all pixel points of the pristine LMR and LMR@0.5% APO samples are consistent with the XANES curves obtained by conventional transmission-mode XANES before and after long-term cycling. This indicates that the differences in the bulk oxidation states of LMR particles and enhancement of cycling stability by the $AlPO_4$-coating layer are closely related to the uniformity of the Mn reaction. After 200 cycles, the 2D oxidation-state mapping of Mn in the pristine LMR sample (Fig. 5b) shows a decrease

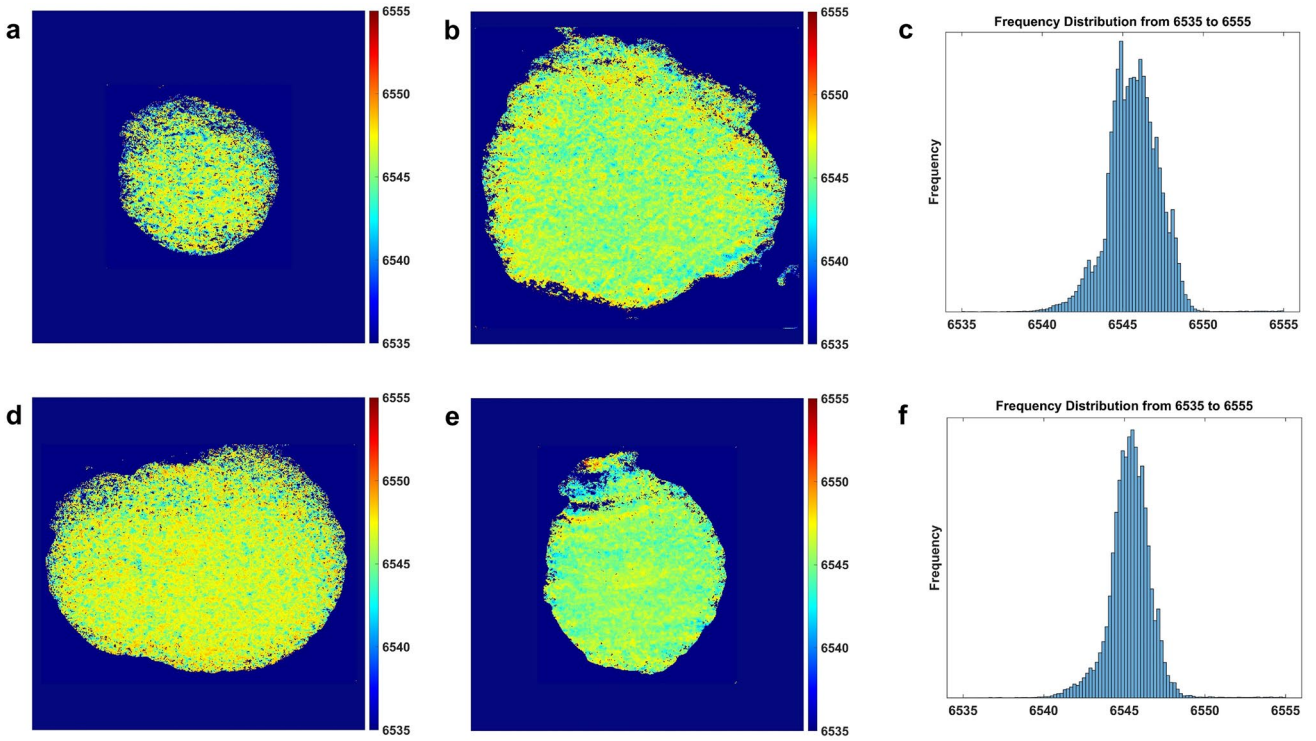

Fig. 5 (Color online) 2D valence-state mappings (pixel scale: 30 nm) at Mn K-edge of the pristine **a** LMR and **d** LMR@0.5% APO samples; 2D valence-state mappings at Mn K-edge of the cycled **b** LMR and **e** LMR@0.5% APO samples. Pixel energy-distribution histogram of **c** LMR and **f** LMR@0.5% APO samples

in the oxidation state at the center position corresponding to the bulk of the sample. A clear enrichment of high-valence Mn is observed at the edge positions corresponding to the sample surface, which leads to a slight increase in the average oxidation state. This result is consistent with the difference between the bulk and surface regions of the samples obtained from hard and soft X-ray absorption spectroscopy. This indicates that during the extended cycling process, the continuous disproportionation reaction leads to the dissolution of lower-valence Mn, resulting in significant aging-induced deactivation of Mn on the material surface. This deactivation slows the reaction kinetics and causes detachment from the conductive network, ultimately leading to rapid capacity decay. The 2D oxidation-state mapping of Mn in the cycled LMR@0.5% APO sample (Fig. 5e) shows consistent color regions distributed evenly in the whole secondary particles, which indicates that no obvious chemical phase separation of Mn occurs after 200 cycles. This implies that the aging states of Mn are uniform, signifying the isotropic reactivity of Mn in LMR@0.5% APO during cycling, which can be attributed to the protective effects of the $AlPO_4$-coating layer. As shown in Fig. 5c, f, by statistically analyzing the pixels corresponding to different oxidation states in the 2D oxidation-state distribution mappings of Mn, we can directly observe a clear coexistence of multiple valence states in the pristine LMR sample after cycling. This demonstrates that the distribution of Mn valence states is nonuniform. In contrast, in the LMR@0.5% APO sample, the valence-state distribution of different pixels is more concentrated with only one center, demonstrating a significant improvement in the uniformity of the reaction.

3.5 Structural changes caused by anionic redox reactions at high voltage investigated by synchrotron-based X-ray absorption spectroscopy

The oxygen-oxidation reaction in LMR materials at high voltages can provide extraordinary capacity; however, it can also lead to issues such as surface oxygen release, transition-metal reduction, and densification, thereby affecting the electrochemical performance and stability of the materials during subsequent cycles. Therefore, we used both hard and soft XAS to investigate the evolution of the electronic and local coordination structures of the transition-metal and oxygen ions at high voltages before and after surface modification [49–51]. The O K-edge XAS test was carried out at beamline BL02B02 of the SSRF using the combined TEY and TFY modes [27]. In this mode, we can measure the photogenerated current on the material surface and fluorescence

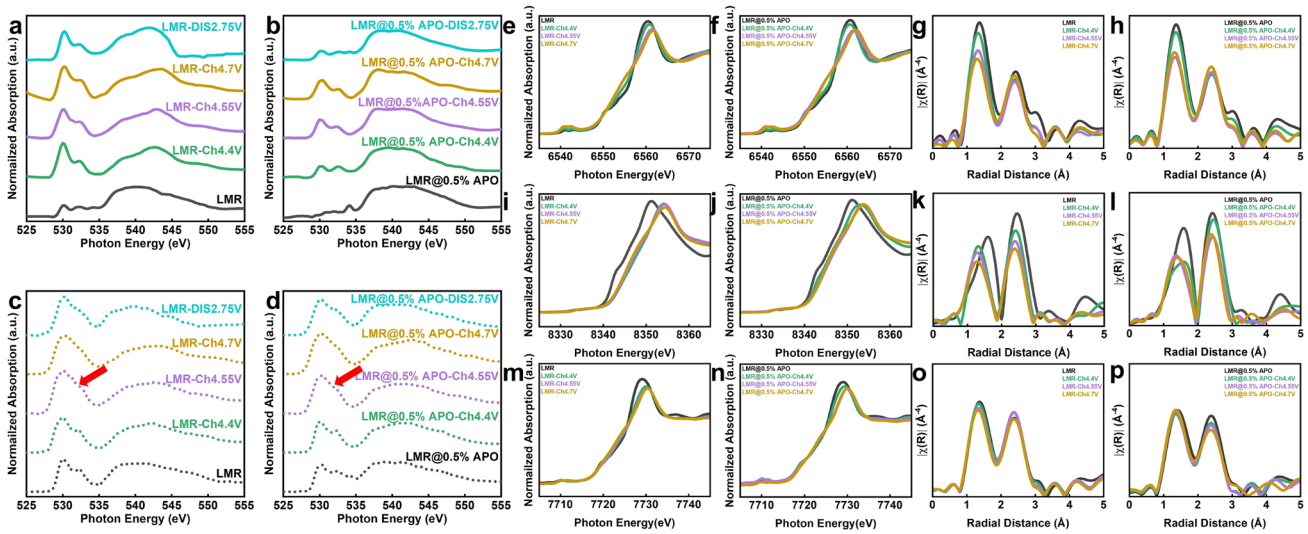

Fig. 6 (Color online) Ex-situ XANES spectra during high-voltage plateau: ex-situ XANES spectra in TEY mode at O K-edge of pristine **a** LMR and **b** LMR@0.5% APO samples. Ex-situ XANES spectra in TFY mode at O K-edge of pristine **c** LMR and **d** LMR@0.5% APO samples. Ex-situ XANES spectra of pristine LMR sample at **e** Mn K-edge, **i** Ni K-edge, and **m** Co K-edge. Ex-situ XANES spectra of LMR@0.5% APO sample at **f** Mn K-edge, **j** Ni K-edge, and **n** Co K-edge. Ex-situ FT-EXAFS of pristine LMR sample at **g** Mn K-edge, **k** Ni K-edge, and **o** Co K-edge. Ex-situ FT-EXAFS of LMR@0.5% APO sample at **h** Mn K-edge, **l** Ni K-edge, and **p** Co K-edge

from the bulk of the material simultaneously; therefore, the information from the surface and bulk of the materials can be obtained simultaneously [41]. LMR materials are prone to severe surface oxygen release during cycling; hence, simultaneous tracking of O in both the surface and bulk is crucial for the mechanistic study of LMR materials. As shown in Fig. 6a, c, the broad spectral features above 535 eV are related to the transitions from O 1 s to the TM 4sp hybridized O 2p states. The two pre-edge peaks at approximately 530 and 532 eV are attributed to the transitions from O 1 s to the unoccupied TM d orbitals [52]. The pristine LMR sample surface exhibits a distinct signal of the cathode electrolyte interphase layer before the reaction. Within this signal, the pre-edge peak corresponding to the hybridization of the transition-metal 3d orbitals has a low intensity, and a carbonate-species peak is observed at 534 eV [53]. Owing to the gradual oxidation of the transition-metal ions, the degree of hybridization between the TM 3d and O 2p bands increases as charging proceeds, resulting in a significant increase in the intensity of the pre-edge peaks corresponding to the 1 s to t_{2g} and e_g transitions. When the pristine LMR sample is charged to a high-voltage plateau (>4.4 V) and undergoes oxygen-oxidation reactions, lattice oxygen-oxidation signals (531 eV) can be detected on the sample surface. However, compared with the bulk phase signals obtained in the TFY mode (Fig. 6c), a significant loss of oxidized lattice oxygen is observed. This surface oxygen release corresponds to surface Mn reduction at high voltages observed at the Mn L-edge, which further facilitates the reduction of Mn and potentially leads to further disproportionation during the discharge process. When discharged to 2.75 V, the sXAS spectrum of the pristine LMR sample differs from its original state and still exhibits a strong pre-edge peak. This indicates that many transition-metal ions remain on the surface near the end of the discharge process, corresponding to the dissolution of transition metals observed at the Mn L-edge. In contrast, the LMR@0.5% APO sample shows significantly suppressed surface redox reactions owing to the presence of the $AlPO_4$-coating layer, whereas redox reactions in the bulk phase remain unaffected (Fig. 6b, d). Additionally, no transition-metal ions remain on the surface during the discharge process, demonstrating that the $AlPO_4$-coating layer effectively suppresses the reactivity on the surface of the sample to stabilize the surface structure, inhibiting Mn disproportionation and dissolution at low voltages. The ex-situ Mn, Co, and Ni K-edge XANES spectra in Fig. 6e, f, i, j, m, n, show noticeable differences in the evolution trends of the electronic structure and local coordination structure of the TM ions in the pristine LMR and LMR@0.5% APO samples under high voltage. In both samples, the shift to the right-hand side of the Ni K-edge is more pronounced than the shifts of the Co and Mn K-edges, which is consistent with Ni providing a larger capacity during the first plateau of the charging process. In the pristine LMR sample, the shifts in the Ni, Co, and Mn K-edges during the first charging plateau are larger than those in the LMR@0.5% APO sample, indicating that the $AlPO_4$-coating layer can also alleviate the overly rapid oxidation rate of TM ions in the bulk. This is consistent with the surface information obtained from sXAS mentioned above. During anionic oxidation, the valence

states of the transition metals no longer undergo significant changes. The Fourier transformed EXAFS of the Ni, Co, and Mn K-edges (Fig. 6g, h, k, l, o, p) illustrates that the $AlPO_4$-coating layer stabilizes the coordination structure effectively. The first coordination shell in the FT-EXAFS spectra of transition-metal oxides generally corresponds to TM-O bonds, and the second coordination shell generally corresponds to TM-TM bonds. Thus, as shown in Fig. 6g, h, compared to the pristine sample, the Mn-O and Mn-TM coordination corresponding to the first and second coordination shells, respectively, only undergoes slight, uniform shifts in the LMR@0.5% APO sample. Moreover, as the reaction proceeds, the decrease in the intensity of the coordination peaks is even smaller. This demonstrates that the increase in the local structural disorder is alleviated, which is conducive to stabilizing the bulk structure and inhibiting the migration of transition metals and release of oxygen. In Fig. 6k, l, the Fourier transformed EXAFS curves of the Ni K-edge show that Ni experiences a noticeable leftward shift in its first coordination shell Ni-O coordination peak due to providing a large number of electrons during the charging process. Compared to that of the pristine LMR sample, the Ni coordination structure of the coated sample charged to 4.4 V shows obvious distortion, owing to the retention of some Ni^{3+} in the bulk phase. After the pristine LMR sample is charged to 4.55 V, the Ni-O coordination peak in the sample continues to decrease, indicating progressively severe local structural distortion during the anionic redox process. In contrast, the Ni-O coordination peak in the coated sample exhibits a higher intensity than that in the pristine sample, and no significant change is observed in the intensity of the Ni-O coordination peak in the fully charged state. This indicates that the local structural distortion of Ni in the LMR@0.5% APO sample is effectively suppressed during the anionic redox stage. In Fig. 6o and p, the Co-O coordination also undergoes similar changes during anionic redox process. The changes in its coordination structure are minor compared to those of the pristine LMR sample, especially after being fully charged. The differences in the bond-length changes between the Ni and Co ions can be attributed to the different electronic structures of the Ni^{2+} and Co^{3+} ions. The strong σ interaction of the Ni-O bond renders it more sensitive to redox reactions than the weak π interaction of the Co-O bond [33]. In conclusion, the $AlPO_4$ coating layer can effectively stabilize the bulk structure of LMR materials under high voltages and alleviate local structural distortion and oxygen loss, which leads to structural collapse from the surface to the bulk during subsequent cycling, thereby effectively enhancing the electrochemical performance of the material.

4 Conclusion

A facile encapsulation strategy of precipitating a nanoscale amorphous $AlPO_4$-coating layer on an LMR cathode was developed. Without altering the bulk structure, the nanoscale amorphous $AlPO_4$ coating effectively enhanced the initial discharge capacity and Coulombic efficiency of the cathode, effectively suppressing sharp capacity decay during the extended cycling process and improving its cycling stability. By integrating complementary synchrotron-based characterization techniques, we conducted a detailed analysis of the mechanism by which the $AlPO_4$-coating layer enhances the electrochemical performance. Using sXAS in the TEY and TFY modes to precisely characterize the unoccupied electronic structure on the surface of the materials and compare the electronic structures of the material surface with its bulk phase, the $AlPO_4$-coating layer was proven to effectively enhance the surface structure of the material. Without affecting the redox reactions in the bulk, it suppressed the anionic and cationic redox reactions on the surface of LMR material, effectively alleviating irreversible oxygen release on the surface. Moreover, the $AlPO_4$-coating layer prevents direct contact between the cathode and electrolyte and reduces the dissolution of Mn^{2+} at the interface caused by side reactions. The 2D distribution of the Mn oxidation state was analyzed using the advanced TXM-XANES technique to clarify why the $AlPO_4$-coating layer mitigates the rapid capacity decay of LMR materials. The specific mechanism by which the $AlPO_4$-coating layer alleviates the rapid capacity decay of LMR materials is by enhancing the reaction uniformity of Mn and preventing the deactivation of surface Mn. Furthermore, ex-situ studies utilizing XANES and FT-EXAFS techniques demonstrated that the $AlPO_4$-coating layer can improve the structural stability of LMR materials at high voltages, thereby enhancing their capacity and stability. In summary, electrochemical testing and detailed physical characterization was used to prove that the $AlPO_4$ -coating layer is a simple and effective method to improve the electrochemical performance of LMR materials. The specific regulatory mechanism of the $AlPO_4$-coating layer on the LMR material performance was elucidated by combining various synchrotron-based techniques to analyze the structural evolution of cathode materials from the surface to the bulk. This methodology can also provide guidance for the subsequent development and mechanism studies of cathode materials.

Supplementary Information The online version contains supplementary material available at https://doi.org/10.1007/s41365-025-01658-8.

Author Contributions All authors contributed to the study conception and design. Material preparation, data collection, and analysis were performed by Zhong-Qin Dai, Huan Chen, and Zhao-Yin Wen. The first draft of the manuscript was written by Zhong-Qin Dai, and all authors

commented on previous versions of the manuscript. All authors read and approved the final manuscript.

Data Availability The data that support the findings of this study are openly available in Science Data Bank at https://cstr.cn/31253.11.sciencedb.j00186.00262 and https://doi.org/10.57760/sciencedb.j00186.00262.

Declarations

Conflict of interest The authors declare that they have no conflict of interest.

References

1. M. Li, J. Lu, Z. Chen et al., 30 years of Lithium-ion batteries. Adv. Mater. **30**, 1800561 (2018). https://doi.org/10.1002/adma.201800561
2. Z. Shen, J. Huang, Y. Xie et al., Solid electrolyte interphase on lithium metal anodes. ChemSusChem **17**, e202301777 (2024). https://doi.org/10.1002/cssc.202301777
3. J.R. Croy, M. Balasubramanian, K.G. Gallagher et al., Review of the US department of energy's "Deep Dive" effort to understand voltage fade in Li- and Mn-rich cathodes. Acc. Chem. Res. **48**, 2813–2821 (2015). https://doi.org/10.1021/acs.accounts.5b00277
4. D.-H. Seo, J. Lee, A. Urban et al., The structural and chemical origin of the oxygen redox activity in layered and cation-disordered Li-excess cathode materials. Nat. Chem. **8**, 692–697 (2016). https://doi.org/10.1038/nchem.2524
5. W.E. Gent, K. Lim, Y. Liang et al., Coupling between oxygen redox and cation migration explains unusual electrochemistry in Lithium-rich layered oxides. Nat. Commun. **8**, 2091 (2017). https://doi.org/10.1038/s41467-017-02041-x
6. B. Cao, T. Li, W. Zhao et al., Correlating rate-dependent transition metal dissolution between structure degradation in Li-rich layered oxides. Small **19**, 2301834 (2023). https://doi.org/10.1002/smll.202301834
7. L. Wang, T. Liu, A. Dai et al., Reaction inhomogeneity coupling with metal rearrangement triggers electrochemical degradation in lithium-rich layered cathode. Nat. Commun. **12**, 5370 (2021). https://doi.org/10.1038/s41467-021-25686-1
8. J. Betz, J.P. Brinkmann, R. Nölle et al., Cross talk between transition metal cathode and Li metal anode: unraveling its influence on the deposition/dissolution behavior and morphology of Lithium. Adv. Energy Mater. **9**, 1900574 (2019). https://doi.org/10.1002/aenm.201900574
9. G. Assat, D. Foix, C. Delacourt et al., Fundamental interplay between anionic/cationic redox governing the kinetics and thermodynamics of lithium-rich cathodes. Nat. Commun. **8**, 2219 (2017). https://doi.org/10.1038/s41467-017-02291-9
10. H.Y. Asl, A. Manthiram, Proton-induced disproportionation of Jahn-Teller-active transition-metal ions in oxides due to electronically driven lattice instability. J. Am. Chem. Soc. **142**, 21122–21130 (2020). https://doi.org/10.1021/jacs.0c10044
11. S. Zhang, H. Gu, T. Tang et al., In situ encapsulation of the nanoscale Er_2O_3 phase to drastically suppress voltage fading and capacity degradation of a Li- and Mn-rich layered oxide cathode for Lithium ion batteries. ACS Appl. Mater. Interfaces **9**, 33863–33875 (2017). https://doi.org/10.1021/acsami.7b09002
12. J. Peng, Y. Li, Z. Chen et al., Phase compatible $NiFe_2O_4$ coating tunes oxygen redox in Li-rich layered oxide. ACS Nano **15**, 11607–11618 (2021). https://doi.org/10.1021/acsnano.1c02023
13. J. Zhang, Q. Wang, S. Li et al., Depth-dependent valence stratification driven by oxygen redox in lithium-rich layered oxide. Nat. Commun. **11**, 6342 (2020). https://doi.org/10.1038/s41467-020-20198-w
14. A. Deb, U. Bergmann, E.J. Cairns et al., X-ray absorption spectroscopy study of the Li_xFePO_4 cathode during cycling using a novel electrochemical in situ reaction cell. J. Synchrotron Radiat. **11**, 497–504 (2004). https://doi.org/10.1107/s0909049504024641
15. J. Li, Y. Li, P.K. Routh et al., Comparative analysis of XANES and EXAFS for local structural characterization of disordered metal oxides. J. Synchrotron Radiat. **28**, 1511–1517 (2021). https://doi.org/10.1107/S1600577521007025
16. L. Du, X. Du, Q. Wang et al., Design of the new soft X-ray beamline for in situ analysis of energy materials at national synchrotron radiation laboratory. Nucl. Instrum. Methods Phys. Res. Sect. A **877**, 65–68 (2018). https://doi.org/10.1016/j.nima.2017.09.045
17. G. Margaritondo, F. Cerrina, Overview of soft-X-ray photoemission spectromicroscopy. Nucl. Instrum. Methods Phys. Res. Sect. A **291**, 26–35 (1990). https://doi.org/10.1016/0168-9002(90)90028-5
18. C. Rau, A. Somogyi, A. Simionovici, Microimaging and tomography with chemical speciation. Nucl. Instrum. Methods Phys. Res. Sect. B **200**, 444–450 (2003). https://doi.org/10.1016/S0168-583X(02)01737-8
19. T. Alemu, F.M. Wang, In situ electrochemical synchrotron radiation for Li-ion batteries. J. Synchrotron Radiat. **25**, 151–165 (2018). https://doi.org/10.1107/s1600577517015533
20. R.Z. Tai, Z.T. Zhao, Overview of SSRF phase-II beamlines. Nucl. Sci. Tech. **35**, 137 (2024). https://doi.org/10.1007/s41365-024-01487-1
21. H.-L. Xie, B. Deng, G.-H. Du et al., Methodology development and application of X-ray imaging beamline at SSRF. Nucl. Sci. Tech. **31**, 102 (2020). https://doi.org/10.1007/s41365-020-00805-7
22. C.R. Wu, X.P. Fang, X.W. Guo et al., Surface modification of $Li_{1.2}Mn_{0.54}Co_{0.13}Ni_{0.13}O_2$ with conducting polypyrrole. J. Power Sources **231**, 44–49 (2013). https://doi.org/10.1016/j.jpowsour.2012.11.138
23. H. Yu, X.J. Wei, J. Li et al., The XAFS beamline of SSRF. Nucl. Sci. Tech. **26**, 050102 (2015). https://doi.org/10.13538/j.1001-8042/nst.26.050102
24. Z.H. Chen, F.F. Sun, Y. Zou et al., Design of wide-range energy material beamline at the Shanghai synchrotron radiation facility. Nucl. Sci. Tech. **29**, 26 (2018). https://doi.org/10.1007/s41365-018-0356-6
25. C.P. Wang, Z.J. Xu, H.G. Liu et al., Soft X-ray ptychography method at SSRF. Nucl. Sci. Tech. **28**, 74 (2017). https://doi.org/10.1007/s41365-017-0227-6
26. Z.L. Juan, X.Z. Jian, Z.X. Zhi et al., Latest advances in soft X-ray spectromicroscopy at SSRF. Nucl. Sci. Tech. **26**, 040101 (2015). https://doi.org/10.13538/j.1001-8042/nst.26.040101
27. X. Meng, Z. Guo, Y. Wang et al., Design and performance of bending-magnet beamline BL02B at the SSRF. J. Synchrotron Radiat. **26**, 543–550 (2019). https://doi.org/10.1107/S1600577518018179
28. B. Ravel, M. Newville, ATHENA, ARTEMIS, HEPHAESTUS: data analysis for X-ray absorption spectroscopy usssing IFEFFIT. J. Synchrotron Radiat. **12**, 537–541 (2005). https://doi.org/10.1107/S0909049505012719
29. L. Zhang, F. Tao, J. Wang et al., The 3D nanoimaging beamline at SSRF. Nucl. Sci. Tech. **34**, 201 (2023). https://doi.org/10.1007/s41365-023-01347-4
30. A.T. Appapillai, A.N. Mansour, J. Cho et al., Microstructure of $LiCoO_2$ with and without "$AlPO_4$" nanoparticle coating: combined STEM and XPS studies. Chem. Mater. **19**, 5748–5757 (2007). https://doi.org/10.1021/cm0715390

31. F. Wu, X. Zhang, T. Zhao et al., Multifunctional $AlPO_4$ coating for improving electrochemical properties of low-cost Li $Li_{0.2}Fe_{0.1}Ni_{0.15}Mn_{0.55}O_2$ cathode materials for Lithium-ion batteries. ACS Appl. Mater. Interfaces **7**, 3773–3781 (2015). https://doi.org/10.1021/am508579r
32. Q. Guo, J. Huang, Z. Liang et al., The use of a single-crystal nickel-rich layered NCM cathode for excellent cycle performance of lithium-ion batteries. New J. Chem. **45**, 3652–3659 (2021). https://doi.org/10.1039/d0nj05914e
33. B. Li, Z.Q. Zhuo, L.T. Zhang et al., Decoupling the roles of Ni and Co in anionic redox activity of Li-rich NMC cathodes. Nat. Mater. **22**, 1370–1379 (2023). https://doi.org/10.1038/s41563-023-01679-x
34. J. Wu, Q. Li, S. Sallis et al., Fingerprint oxygen redox reactions in batteries through high-efficiency mapping of resonant inelastic X-ray scattering. Condens. Matter **4**, 5 (2019). https://doi.org/10.3390/condmat4010005
35. J. Zheng, M. Gu, J. Xiao et al., Functioning mechanism of AlF_3 coating on the Li- and Mn-rich cathode materials. Chem. Mater. **26**, 6320–6327 (2014). https://doi.org/10.1021/cm502071h
36. H. Wei, Y. Liu, Y. Luo et al., Regulation of anion redox activity via solid-acid modification for highly stable Li-rich Mn-based layered cathodes. Adv. Funct. Mater. **34**, 2307583 (2024). https://doi.org/10.1002/adfm.202307583
37. S. Li, R. Hu, T. Hu et al., Interpretation of the pre-edge X-ray absorption fine structures in MnO. Nucl. Sci. Tech. **14**, 153–156 (2003)
38. F.W. Lytle, The EXAFS family tree: a personal history of the development of extended X-ray absorption fine structure. J. Synchrotron Radiat. **6**, 123–134 (1999). https://doi.org/10.1107/s0909049599001260
39. C.F. Petersburg, R.C. Daniel, C. Jaye et al., Soft X-ray characterization technique for Li batteries under operating conditions. J. Synchrotron Radiat. **16**, 610–615 (2009). https://doi.org/10.1107/S0909049509025710
40. M. Watanabe, T. Ejima, N. Miyata et al., Studies of multilayer structure in depth direction by soft X-ray spectroscopy. Nucl. Sci. Tech. **17**, 257–267 (2006). https://doi.org/10.1016/S1001-8042(06)60048-1
41. W.L. Yang, T.P. Devereaux, Anionic and cationic redox and interfaces in batteries: advances from soft X-ray absorption spectroscopy to resonant inelastic scattering. J. Power Sources **389**, 188–197 (2018). https://doi.org/10.1016/j.jpowsour.2018.04.018
42. E. Yin, A. Grimaud, G. Rousse et al., Structural evolution at the oxidative and reductive limits in the first electrochemical cycle of $Li_{1.2}Ni_{0.13}Mn_{0.54}Co_{0.13}O_2$. Nat. Commun. **11**, 1252 (2020). https://doi.org/10.1038/s41467-020-14927-4
43. T. Liu, A. Dai, J. Lu et al., Correlation between manganese dissolution and dynamic phase stability in spinel-based lithium-ion battery. Nat. Commun. **10**, 4721 (2019). https://doi.org/10.1038/s41467-019-12626-3
44. N. Abharana, C. Nayak, K. K. Halankar et al., First results of in-situ X-ray absorption spectroscopy study on charging-discharging cycles of Lithium ion battery at Indus-2 SRS. Nucl. Instrum. Methods Phys. Res. Sect. A **972**, 164032 (2020). https://doi.org/10.1016/j.nima.2020.164032
45. T. Nonaka, C. Okuda, Y. Ukyo et al., In situ XAFS study on cathode materials for Lithium-ion batteries. J. Synchrotron Radiat. **8**, 869–871 (2001). https://doi.org/10.1107/s0909049500017076
46. S.J. Gurman, Interpretation of exafs data. J. Synchrotron Radiat. **2**, 56–63 (1995). https://doi.org/10.1107/s0909049594009179
47. F. Meirer, J. Cabana, Y. Liu et al., Three-dimensional imaging of chemical phase transformations at the nanoscale with full-field transmission X- ray microscopy. J. Synchrotron Radiat. **18**, 773–781 (2011). https://doi.org/10.1107/s0909049511019364
48. Y. Liu, F. Meirer, P.A. Williams et al., TXM-Wizard: a program for advanced data collection and evaluation in full-field transmission X-ray microscopy. J. Synchrotron Radiat. **19**, 281–287 (2012). https://doi.org/10.1107/S0909049511049144
49. Y. Uchimoto, H. Sawada, T. Yao, Changes in electronic structure by Li ion deintercalation in $LiCoO_2$ from cobalt L-edge and oxygen K-edge XANES. J. Synchrotron Radiat. **8**, 872–873 (2001). https://doi.org/10.1107/S0909049500020938
50. T. Zhao, W. Chu, H. Zhao et al., XAS study of $LiFePO_4$ synthesized by solid state reactions and hydrothermal method. Nucl. Instrum. Methods Phys. Res. Sect. A **619**, 122–127 (2010). https://doi.org/10.1016/j.nima.2010.01.066
51. U. Chandra, J. C. Jan, J. W. Chiou et al., Electronic structures of $La_{0.7-x}Cs_xCa_{0.}MnO_3$ probed by X-ray absorption spectroscopy. Nucl. Instrum. Methods Phys. Res. Sect. B **199**, 185-189 (2003). https://doi.org/10.1016/S0168-583X(02)01423-4
52. J. Lee, D.A. Kitchaev, D.-H. Kwon et al., Reversible Mn^{2+}/Mn^{4+} double redox in lithium-excess cathode materials. Nature **556**, 185 (2018). https://doi.org/10.1038/s41586-018-0015-4
53. G. Liang, V. K. Peterson, Z. Wu et al., Crystallographic-site-specific structural engineering enables extraordinary electrochemical performance of high-voltage $LiNi_{0.5}Mn_{1.5}O_4$ spinel cathodes for Lithium-ion batteries. Adv. Mater. **33**, 2101413 (2021). https://doi.org/10.1002/adma.202101413